

www.acsami.org Research Article

Multiscale Modeling of Sintering-Driven Conductivity in Large Nanowire Ensembles

Harish Devaraj, Qi Tian, Weihong Guo, and Rajiv Malhotra*



Cite This: ACS Appl. Mater. Interfaces 2021, 13, 56645-56654



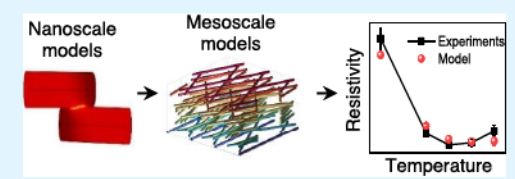
ACCESS I

Metrics & More



Supporting Information

ABSTRACT: Thermally driven sintering is widely used to enhance the conductivity of metal nanowire (NW) ensembles in printed electronics applications, with rapid nonisothermal sintering being increasingly employed to minimize substrate damage. The rational design of the sintering process and the NW morphology is hindered by a lack of mechanistically motivated and computationally efficient models that can predict sintering-driven neck growth between NWs and the resulting change in ensemble conductivity. We present a de



novo modeling framework that, for the first time, links rotation-regulated nanoscale neck growth observed in atomistic simulations to continuum conductivity evolution in inch-scale NW ensembles via an analytical neck growth model and master curve formulations of neck growth and resistivity. This framework is experimentally validated against the emergent intense pulsed light-sintering process for Ag NWs. An ultralow computational effort of 0.2 CPU-h is achieved, 4—10 orders of magnitude reduction as compared to the state of the art. We show that the inherent local variation in the relative NW orientation within an ensemble drives significant junction-specific differences in neck growth kinetics and junction resistivity. This goes beyond the conventional assumption that the neck growth kinetics is the same at all the NW junctions in an ensemble, with significant implications on how nanoscale neck growth affects ensemble-scale conductivity. Through its low computational time, easy and rapid recalibration, and experimental relevance, our framework constitutes a much-needed foundational enabler for a priori design of the sintering process and the NWs.

KEYWORDS: nanowires, sintering, conductivity, molecular dynamics, multiscale model

1. INTRODUCTION

Metal nanowires (NWs) are of increasing interest for printing electrically conductive structures in planar, 1-10 conformal, 11,3 and structural 13,14 electronics. Such NWs, for example, of silver and nickel, are commonly printed using inkjet, roll-to-roll, and screen-based methods. While the NW geometry and ensemble morphology affect the as-printed properties of the ensemble, a subsequent sintering step that reduces resistivity via inter-NW neck growth is often necessary to obtain high electrical conductivity for many applications. 15-17 Conventional isothermal oven sintering is limited by substrate damage, an issue that is mitigated at the cost of throughput using low temperatures over longer time periods. 18 Recently developed nonisothermal sintering processes use energy sources like lasers, 19-21 intense pulsed light, 21-24 and electrical current 25 to rapidly and selectively heat the printed NW ensembles. This enables rapid NW sintering while avoiding substrate damage. These processes also achieve high throughput and scalability, for example, intense pulsed light sintering (IPL) can achieve conductivity as high as $18 \times 10^{\circ}$ S/m over a 1 ft. \times 1 in. area in as little as 2.5 s. 26-29 A common thread in the abovementioned processes is that sintering is driven by heat, albeit the mechanism and the rate at which this heat is created might be different. Sintering-driven neck growth and the resulting change in ensemble conductivity are primarily dependent on the temperature history imposed by the sintering process and

the NW diameter.³⁰ Thus, the rational design to achieve the desired conductivity with minimal substrate damage requires models that link the NW size and the thermal history during sintering to the ensemble conductivity via the physical state of inter-NW neck growth.

Conductivity models for as-printed ensembles do not explicitly consider sintering-driven neck growth. ^{32–35} Phenomenological models that explicitly consider neck growth have modeled the ensemble conductivity as a function of the instantaneous temperature. ^{27,30,36} This ignores the fact that the temperature history and not just the instantaneous temperature drive neck growth, especially under nonisothermal sintering conditions. ^{37,38} As-printed NW ensembles typically consist of multiple layers of stacked NWs with junction-to-junction variations in the relative NW orientation (Figure 1a–d). Recent molecular dynamics (MD) simulations have shown significant local rotation of the NWs during sintering, which tends to align the NWs to reduce the total surface energy (Figure 1e). ³¹ The amount of this rotation depends on the

Received: August 29, 2021 Accepted: November 2, 2021 Published: November 16, 2021





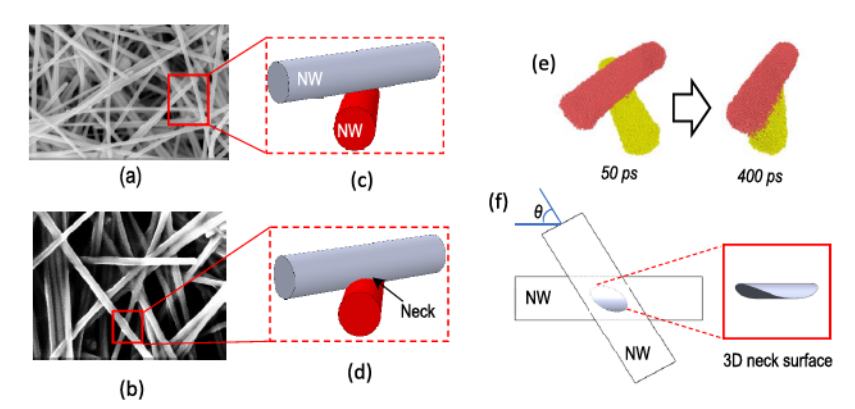


Figure 1. Micrographs of NW networks (a) as-printed and (b) after sintering, from experiments described later in this work. Schematic of NW configurations in (c) as-printed and (d) sintered states. (e) Snapshots of NW rotation during sintering from MD simulations. Reproduced with permission from reference.³¹ Copyright 2020 American Chemical Society. (f) Schematic of instantaneous orientation θ and the 3D neck formed between sintering NWs.

NW radius and the junction-specific value of the initial orientation angle θ (Figure 1f). The rotation drives greater inter-NW neck growth and higher reduction in junction resistivity than those expected from purely geometric considerations. These atomistic simulations have also shown that the neck formed between NWs is anisotropic in nature, that is, the neck interface is a three-dimensional (3D) hyperbolic paraboloid surface (Figure 1f).²⁸ This is unlike the typical two-dimensional (2D) circular neck surface that is created between sintering nanospheres. Because the neck size dictates the junction resistance, incorporating the rotationregulated growth of 3D inter-NW necks is crucial for any physically motivated model of sintering-driven conductivity in NW ensembles. However, computational limitations do not allow the direct use of MD for realistic NW radii (10-100 s of nm), for practical NW ensembles that consist of numerous NWs, and for experimentally relevant sintering durations. There is a need to create mechanistically motivated models that link the NW size, thermal history, and conductivity on realistic time and length scales to eliminate the current reliance on the experimental trial-and-error approach for designing the sintering process and the NW radius.

This study develops a computationally efficient modeling framework that, for the first time, incorporates atomistic insights into capturing temperature-history-dependent neck growth and electrical conductivity in inch-scale NW ensembles over experimentally relevant time scales. The key modeling components of this framework are (a) an analytical model of neck growth between NW pairs based on fundamental conservation equations and mechanistic observations from MD simulations; (b) master neck growth curves (MNCs) for the scalable prediction of junction-specific fusion in multi-NW ensembles, derived using the abovementioned analytical model; (c) master resistivity curves (MRCs) for the scalable prediction of electrical conductivity in sintered NW ensembles, derived using the MNCs, graph theory, and electrical finite element analysis (FEA). This framework is experimentally validated against the conductivity evolution for inch-scale Ag NW films exposed to varying nonisothermal temperature histories in the increasingly popular IPL process. The impact of our framework on enabling design-compatible computational capabilities and new physical insight is discussed. While the focus of this work is on Ag NWs due to their wide use in printed electronics, our framework is also extensible to other metallic NWs. We now discuss the approach and results of each modeling component, followed by a demonstration and discussion of the predictive capabilities of the entire framework.

2. MODELING APPROACH AND RESULTS

2.1. Analytical Neck Growth Model. The first component of our framework is an analytical model of neck growth between stacked and nonaligned NW pairs (Figure 1c). This model assumes that the change in ensemble resistivity during sintering is solely due to inter-NW neck growth. It also incorporates the following mechanistic insights from our past MD simulations of isothermal sintering between Ag NW pairs. First, the neck boundary is modeled as a 3D curve, as shown in Figure 1f. Second, because of NW rotation, the diffusion coefficients corresponding to neck growth and the virtual torque corresponding to NW rotation are functions of the NW radius R, instantaneous orientation angle θ , and the sintering temperature T. Readers are referred to this past work for further details of MD simulations. 31

We assume a single mechanism of neck growth, that is, shrinkage δ between the NWs with a corresponding diffusion coefficient D_{eff} . The specific surface energy γ_s and atomic mobility are assumed to be isotropic along the neck boundary. The normal stress on the neck surface due to atomic diffusion is assumed to be symmetric about the center of the neck's surface. The major and minor axes of the planar neck area measured from MD simulations, that is, A and B, respectively, are geometrically related to the instantaneous θ and δ and to the constant NW radius R, as described in the Supporting Information. This planform measurement ignores the nonplanar 3D nature of the inter-NW neck. Thus, we use a perturbation parameter $\varepsilon = \delta/k(A+B)$ to obtain an effective elliptical neck surface with major axis $a = A(1 + \varepsilon)$ and minor axis $b = B(1 + \varepsilon)$. The value of the constant $k \approx 9$ is based on equating the perimeter of the effective ellipse to that of the 3D neck. This allows for the incorporation of the 3D shape of the neck into the governing equations for the evolution of δ and θ . These governing equations are derived using fundamental conservation equations in conjunction with the abovementioned assumptions as follows. 40-42

The atomic diffusive flux j across the neck surface is related to the normal stress σ on the neck boundary via energy conservation (eq 1), where T is the constant temperature, Ω is

the atomic volume of Ag, and k is the Boltzmann constant. σ is proportional to the curvature K of the free neck surface, as shown in eq 2, where γ_s is the specific surface energy of Ag.

$$j = \frac{D_{\text{eff}}\Omega}{kT}\nabla\sigma\tag{1}$$

$$\sigma = \gamma_{\rm s} K \tag{2}$$

K is approximated as $1/\delta$, based on the principle of mass conservation, as described in the Supporting Information. The force normal to the neck surface that causes shrinkage is obtained by integrating σ over the neck area, and it is equal to the force exerted by the surface tension on the neck boundary. The divergence of the diffusive flux is constant because mass flow within the neck surface is assumed to be isotropic. Using these insights along with the symmetric stress condition at the center of the neck and the principle of mass conservation yields the rate expression for δ in eq. 3 (derivation in eqs. S1–S7). Here, P is the perimeter factor of the effective planar ellipse, and ψ is the dihedral angle.

$$\dot{\delta} = \frac{D_{\text{eff}}\Omega}{kT} \frac{P}{\sqrt{ab}} \frac{4\gamma_s}{ab} \left[2K - \frac{P}{ab} \sin(\psi) \right]$$
 (3)

$$\dot{\theta} = \frac{\Gamma}{\eta \pi (a^2 b^2)} \tag{4}$$

To incorporate NW rotation, we treat the evolution of θ as a consequence of a virtual torque Γ applied at the center of the neck. Based on the conservation of angular momentum, and

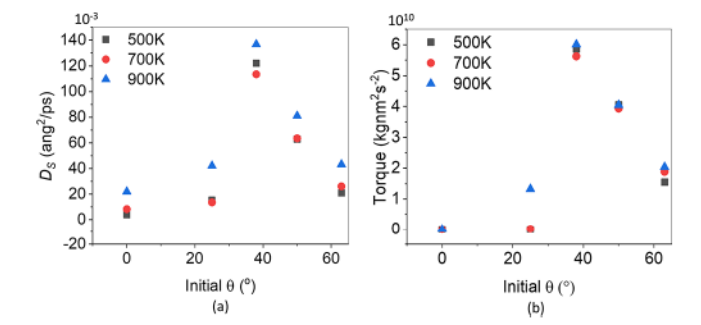


Figure 2. Effect of initial θ and sintering temperature on (a) surface diffusion coefficient D_s and (b) effective torque Γ , from MD simulations for 400 ps sintering time and R = 2.5 nm.

using a rotational drag coefficient denoted as $\eta_1^{41,44}$ the rate expression for θ is shown in eq 4. A detailed derivation of this expression is provided in eqs S8-S11 in the Supporting Information. Eqs 3 and 4 incorporate the coupling between the rotation and neck growth that is observed in MD simulations by coupling δ and θ via a and b. Using the conservation of momentum for a pair of NWs, the above expressions yield a system of equations for an NW pair that is shown in eq 5 (individual NWs denoted by superscripts 1 and 2). 45 θ and δ for an NW pair are updated in a time-marching manner during a sintering simulation, yielding the evolution of the neck area via the change in a and b. Note that eq 5 is extensible to a multi-NW network based on the packing-driven connectivity between the NWs.41

$$\begin{bmatrix} \frac{\pi}{4} \frac{kT}{D_{\text{eff}}\Omega} \frac{ab\sqrt{ab}}{P} & 0 & -\frac{\pi}{4} \frac{kT}{D_{\text{eff}}\Omega} \frac{ab\sqrt{ab}}{P} & 0 \\ 0 & \eta_c \pi ab\sqrt{ab} & 0 & -\eta_c \pi ab\sqrt{ab} \\ -\frac{\pi}{4} \frac{kT}{D_{\text{eff}}\Omega} \frac{ab\sqrt{ab}}{P} & 0 & \frac{\pi}{4} \frac{kT}{D_{\text{eff}}\Omega} \frac{ab\sqrt{ab}}{P} & 0 \\ 0 & -\eta_c \pi ab\sqrt{ab} & 0 & \eta_c \pi ab\sqrt{ab} \end{bmatrix} \begin{bmatrix} \dot{\delta}^1 \\ \dot{\theta}^1_t \\ \dot{\delta}^2 \\ \dot{\theta}^2_t \end{bmatrix} = \begin{bmatrix} \pi \gamma_s \left[2K - \frac{P}{ab} \sin(\psi) \right] \\ \pi \Gamma / \sqrt{ab} \\ -\pi \gamma_s \left[2K - \frac{P}{ab} \sin(\psi) \right] \\ -\pi \Gamma / \sqrt{ab} \end{bmatrix}$$

in which $D_{\rm eff}$ and Γ are given by

$$D_{\text{eff}} = \frac{D_{\text{o}} e^{-E_{\text{a}}/R_{\text{g}}T}}{2\pi\sigma_{\text{D}}} e^{-(\theta - 45)^2/2\sigma_{\text{D}}^2}$$
(6)

$$\Gamma = \frac{g(R, T, \theta_0)}{2\pi\sigma_{\Gamma}} e^{-(\theta - 45)^2/2\sigma_{\Gamma}^2}$$
(7)

The functional expressions for $D_{\rm eff}$ and Γ were based on qualitative observations from MD simulations. MD simulations have shown that surface diffusion dominates inter-NW neck growth. 28,31 Thus, we model Deff as having a similar dependence on R, θ , and T, as observed for the surface diffusion coefficient D_s from MD (e.g., Figure 2a). D_{eff} is cast as having an Arrhenius dependence on T and a Gaussian dependence on θ , as shown in eq 6. $R_{\rm g}$ is the universal gas constant. The standard deviation of the Gaussian function, that is, $\sigma_{\rm D}$, is modeled as a linear function of temperature T (eq S14). The pre-exponential factor D_0 and the activation energy $E_{\rm a}$ are cast as functions of radius R (eq S16 and S17).

The functional dependence of the virtual torque Γ on R, θ , and T is also based on observations from MD simulations (e.g.,

Figure 2b). These numerical values of Γ were calculated from MD simulations based on the moment of inertia of the NW pair and the effective angular acceleration of the NWs over the simulated sintering time. We modeled Γ as a Gaussian function of the instantaneous θ (eq 7). The function g depends on the R, T, and the initial orientation angle θ_0 , as shown in eqs S18— S20. The parameters in the expressions for D_0 , E_a , σ_D , g, and σ_T were manually identified by comparing the neck area predicted using the analytical model to that predicted by MD simulations. These calibration MD simulations performed isothermal sintering between equally sized NWs over a sintering time of 400 ps for a range of NW radii R (2.5-7.5 nm), initial θ (0°-65°), and isothermal sintering temperatures (500-900 K). Figure S3 shows that there is reasonable agreement between the neck sizes predicted by the MD simulations and using the analytical model for the calibration, indicating reasonable model calibration.

This calibrated model was validated against MD simulations corresponding to additional sintering conditions and NW geometries. Figure 3a shows such a comparison for additional combinations of initial θ and sintering temperatures, for the

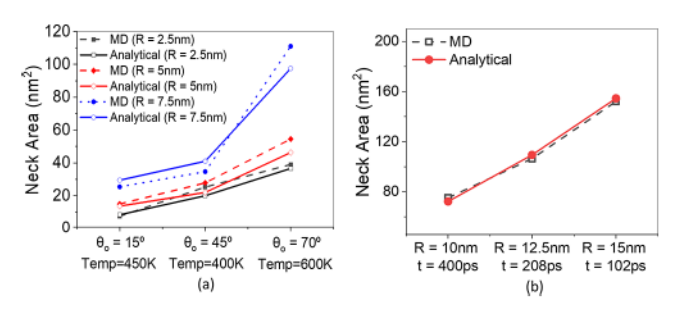


Figure 3. Validation of the analytical model against MD simulations for (a) varying NW radius R, initial angle θ_0 , and sintering temperature for a simulation time of 400 ps (b) varying R beyond the range of radii used for model calibration at a constant temperature of 450 K and initial $\theta = 45^{\circ}$.

same sintering time of 400 ps and the same range of R as that used for calibration. Figure 3b shows the same comparison for NW radii that are well beyond those used for calibration and for additional sintering times. In all these validation cases, the neck size predictions from our analytical model compare well to MD predictions. Thus, our analytical model is extensible to a wider range of thermal histories, initial θ , and NW radii than those used for model calibration. This model does not need to be recalibrated for additional NW radii because A and B, and the parameters for the functions D_0 , E_a , σ_D , g, and σ_T are explicitly parameterized in terms of the NW radii.

Our analytical model reduces the computational effort by 6 orders of magnitude as compared to MD simulations, that is, from 10^3 to 10^{-3} CPU-h. However, this model still cannot be used as a design tool for experimentally relevant NW ensembles. For example, the typical computational effort needed using this model to predict neck growth in a random-packed ensemble of about 100 NWs over a sintering time of 1 μ s is 640 CPU-h. Even with 100 processors, the computational time would be around 6.4 h. Because of numerical stability limitations on the timestep used for solving eq 5, increasing the simulation time to millisecond and second levels used in experiments will increase the computational effort and time to an infeasible point. For example, even in rapid processes like IPL, the typical sintering time is on the order of 100 s of μ s to seconds. The concept of MNCs developed in the next section

leverages the abovementioned analytical model to tackle this issue.

2.2. Master Neck Growth Curves. The second key aspect of our framework is MNCs, which enable computationally feasible modeling of junction-specific neck growth in multi-NW ensembles. Inspired by the use of master curves to predict macroscale porosity in the sintering of microparticles, 40 MNCs predict neck growth between NW pairs as a function of a scalar thermal history parameter Θ (eq 8).

$$\Theta(T, t) = \ln \left[\int_0^{t_s} \frac{1}{T(t)} \exp \left(-\frac{Q}{R_g T(t)} \right) dt \right]$$
 (8)

where Q is the constant activation energy and $t_{\rm s}$ is the total sintering time, with the temperature T cast a function of time t to allow for the incorporation of nonisothermal sintering. The analytical neck growth model was used to predict the neck area for a range of dummy temperature histories. These predictions were used to manually calibrate Q as a function of different initial θ for a specified NW radius R. The generated MNCs level off beyond a certain Θ corresponding to the maximum possible neck growth (e.g., Figure 4). The MNCs also shift to the right with increasing initial θ when the initial θ is lesser than 45° , but shift to the left beyond this critical initial θ value. This reflects the dependence of neck growth on the initial θ as seen in MD simulations (Figure 2).

$$A_n = \chi(\theta_0) e^{\phi(\theta_0) \ln(\Theta)}$$
 (9)

We cast the nonconstant portion of the MNCs as a function of Θ and initial θ (denoted by θ_0 in eq 9). The functional dependence of χ and ϕ on θ_0 was calibrated based on the MNCs for the 25 and 50 nm NW radii that were used in our experiments. Note that the calibration of Q, χ , and ϕ for additional NW radii needs more data from the analytical neck growth model, but it does not need additional runs of the more resource-consuming MD simulations. Using the analytical model for the calibration of MNCs also eliminates the need to conduct MD simulations over sintering times that are computationally inaccessible by MD, but are necessary for covering the wide range of temperature histories needed to derive MNCs.

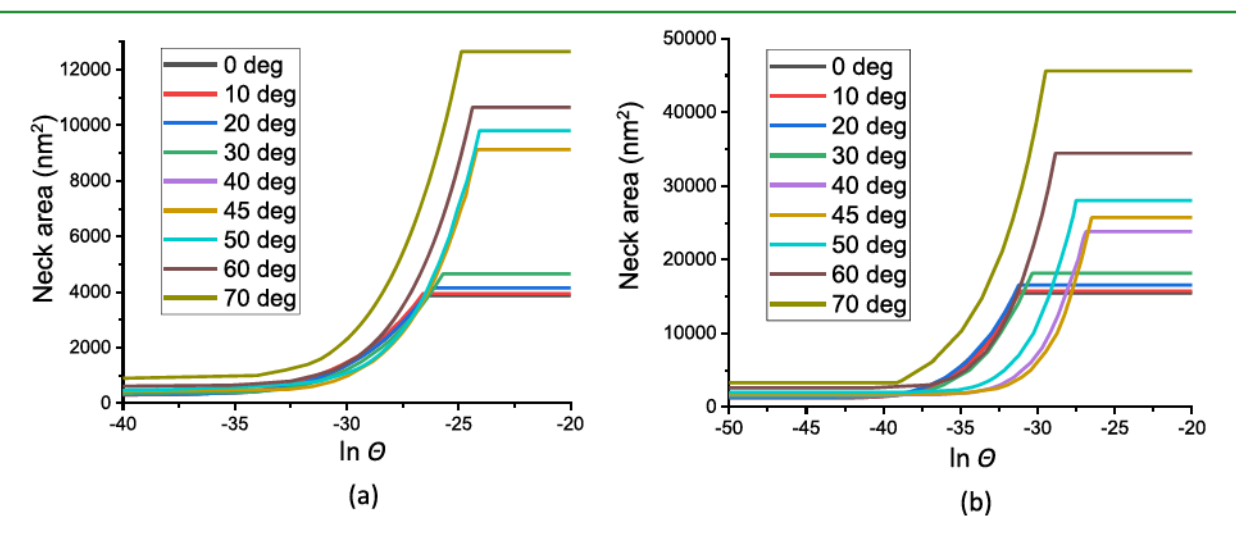


Figure 4. MNCs for NW radius of (a) 25 nm and (b) 50 nm. Legend is for initial angle θ_0 .

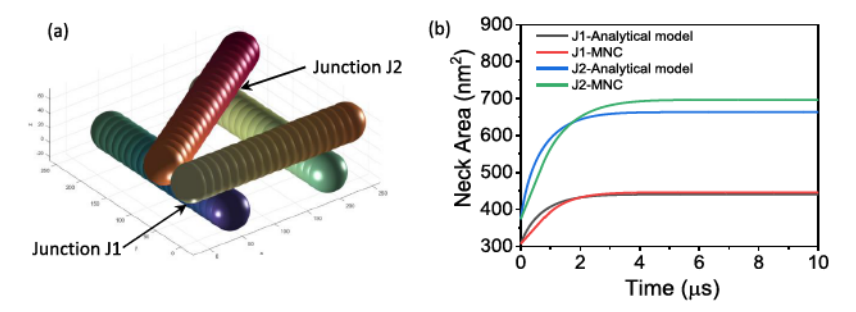


Figure 5. (a) NW ensemble with an NW radius of 25 nm, showing junctions J1 and J2 at which neck growth is predicted. (b) Comparison of neck growth between the direct use of the analytical neck growth model and MNCs for the nonisothermal temperature history shown in Figure S4. Good comparison is obtained between analytical models and MNCs.

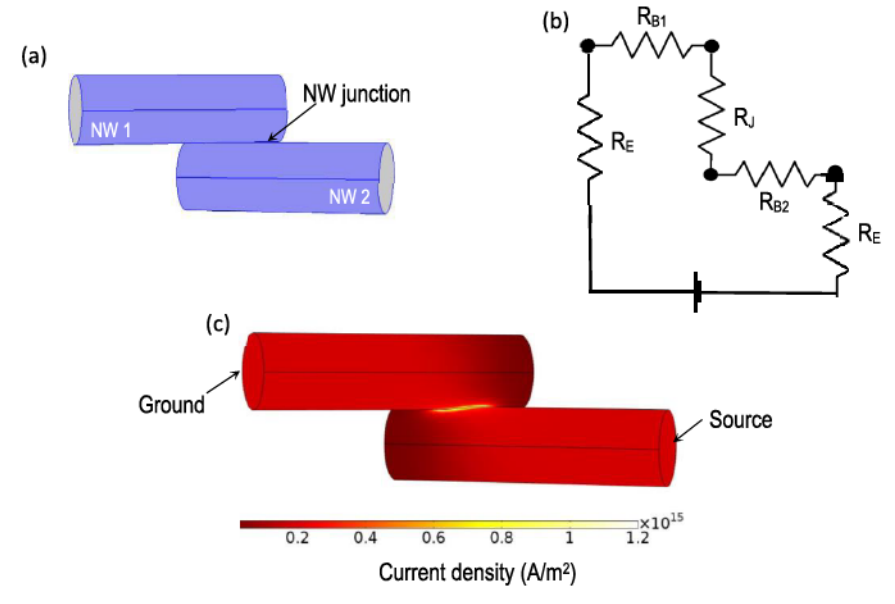


Figure 6. (a) NW pair with inter-NW junction shown (b) corresponding electrical circuit, $R_{\rm B}$ denotes resistances of the bulk of the NWs, $R_{\rm J}$ is the junction resistance, and $R_{\rm E}$ is the external resistance. (c) Predicted current density contours from FEA in COMSOL. Surfaces other than the ground and source were electrically insulated.

Initial validation of the MNCs was performed by comparing predictions of local neck growth to that from the direct use of the analytical neck growth model for a four-NW ensemble (Figure 5a) subjected to a nonmonotonic temperature history (Figure S4). The sintering time and the number of NWs were deliberately chosen to enable the computational feasibility of the analytical model. Figure 5b compares the neck growth at the junctions J1 and J2 in Figure 5a. We note that the MNCs provide quantitatively comparable predictions of the evolution of neck growth.

An interesting insight from this exercise arises from the observation that the initial NW orientations are very different at junctions J1 and J2. Both the analytical model and the MNCs show that neck growth is significantly greater at J2 than at J1. This indicates that in a multi-NW ensemble, the neck growth at different NW junctions depends strongly on the corresponding local NW orientation, which is spatially variable in typical random-packed NW ensembles. Because the junction resistivity depends significantly on the neck area (see the next section), there is an orientation-regulated junction-specific component to the ensemble conductivity. This is a key departure from the state-of-the-art assumption that the dynamics of neck growth and conductivity change are the same at different NW junctions in a multi-NW ensemble. The

above exercise also demonstrates the significant computational advantage achieved by MNCs over the analytical model, let alone the MD simulations. While both the analytical model and the MNCs for this small NW ensemble were executed using seven processors, the computational time was 8 h for the analytical model and 30 s for the MNC. Thus, MNCs enable 1000 times lesser computational effort than the analytical model and 10⁹ times lesser effort than MD simulations. The prediction of conductivity as a function of the thermal history in the experimental validation section provides additional validation of the MNCs.

2.3. Master Resistivity Curves. This section describes the development of MRCs by linking junction-specific neck growth to the electrical conductivity of NW ensembles. The MRCs are derived by first explicitly modeling ensemble resistivity as a function of sintering-driven junction-specific neck growth and then casting the ensemble resistivity as a function of the thermal history parameter Θ . This formulation is based on the insight that because the sintering-induced resistivity change occurs due to a reduction in the junction resistance driven by inter-NW neck growth, and thus, the qualitative dependence of the neck growth on the thermal history should be reflected in the resistivity change. First, we link nanoscale neck growth to ensemble resistivity by

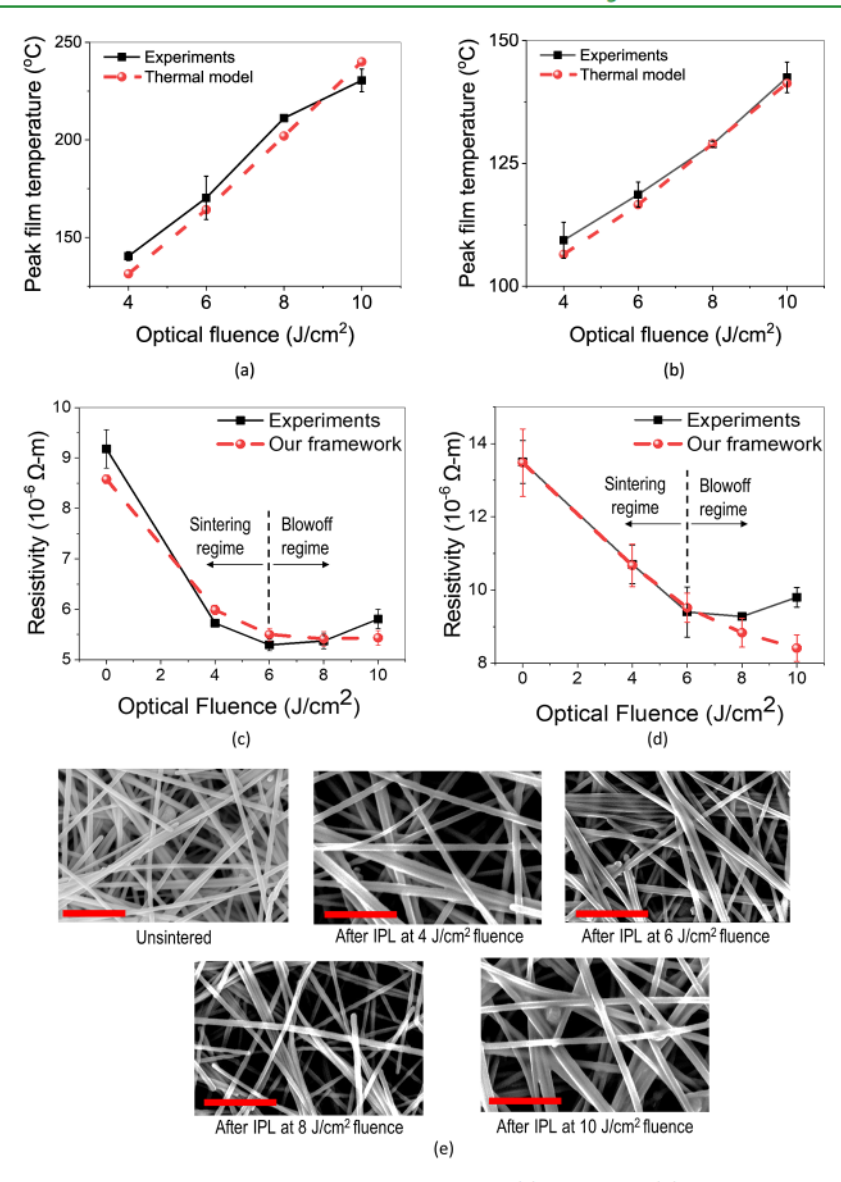


Figure 7. Peak temperature from experiments and thermal FEA for an NW radii of (a) 25 nm and (b) 50 nm. Electrical resistivity from experiments and our modeling framework for NW radii of (c) 25 nm and (d) 50 nm. (e) Representative micrographs of the NW morphology before and after sintering, as a function of the pulse energy used for IPL sintering. All length scales are 1 μ m.

combining an existing analytical model of network resistivity⁴⁶ with electrical FEA. For simplicity, this network resistivity model is described in the context of an NW pair (Figure 6a). The reader is referred to the literature for further computational details on the extension to multi-NW ensembles.⁴⁶

As shown in Figure 6b, this NW pair and indeed any multi-NW network consist of the bulk resistance of the NWs ($R_{\rm B1}$ and $R_{\rm B2}$), inter-NW junction resistances ($R_{\rm J}$), and resistances external to the NW network ($R_{\rm E}$). Electron flow in the ensemble is governed by the network structure and the material properties, which are represented by the incidence N and resistance M matrices, respectively. If i is the number of NW segments and j is the number of NW junctions in the ensemble, then, the diagonal matrix $M_{i,i}$ contains the $R_{\rm B}$, $R_{\rm J}$, and $R_{\rm E}$ values, and the incidence matrix $N_{i,j}$ contains information on the connectivity of the bulk and junction resistances. Using Kirchhoff's current and voltage laws yields the equation for the entire NW network, as shown in eq 10, where V and C denote the voltage and current, respectively,

and subscripts in and out denote electron flow in and out, respectively.

$$\begin{bmatrix} M_{(i,i)} & N_{(i,j)} \\ N_{(j,i)} & 0_{(j,j)} \end{bmatrix} \begin{bmatrix} C_{\text{out}} \\ V_{\text{out}} \end{bmatrix} = \begin{bmatrix} C_{\text{in}} \\ V_{\text{in}} \end{bmatrix}$$
(10)

The functional dependence of $R_{\rm J}$ on NW radius R and neck area A_n was obtained via the FEA of current flow across the junction of an NW pair (Figure 6c). A unit voltage was applied to one end of one NW (source), and the output current was measured on the opposite end of the other NW (ground). Insulation boundary conditions were applied to all other faces of the NWs. The total resistance of these two NW circuit $R_{\rm T}$ was calculated as the reciprocal of the current across the cross-section of any NW. Because the junction and bulk resistances are in series, the corresponding $R_{\rm J}$ was obtained as $R_{\rm T}-R_{\rm B1}-R_{\rm B2}$. Simulations were performed for varying A_n , which was manipulated by changing the orientation θ and shrinkage δ . The NW radius was varied from 5 to 100 nm to examine any potential dependence of $R_{\rm J}$ on the radius. We found that $R_{\rm J}$

does not depend on the NW radius but has a power-law dependence on the neck area A_m , as shown in eq 11. $R_{\rm B}$ was computed using Pouillet's law based on the assumption that the resistivity of the bulk NW material is the same as that of bulk silver (i.e., 1.59 $\mu\Omega$ cm).⁴⁷ $R_{\rm E}$ was ignored because the external resistances in experimental measurements are much lower than $R_{\rm J}$. The output voltage $V_{\rm out}$ in eq 10 was evaluated via matrix inversion by applying the unit voltage and zero source current.⁴⁶

$$R_{\rm J} = 100 A_n^{-0.7} \tag{11}$$

Eqs 10 and 11 were used to derive MRCs for multi-NW ensembles as follows. The ensembles were created using the sequential packing method 48 and an exemplar packed ensemble is shown in Figure S5. Because packing is not the focus of this study, we ignore contact mechanics or wrapping of the NWs around each other for simplicity. The total height of the ensembles was the same as the film thickness measured in experiments. The ensemble width and depth, the number of NWs per layer, and the intralayer spacing between the NWs were iteratively determined for a given NW radius such that the initial ensemble resistivity matched experimental measurements for the unsintered films. A typical ensemble had an inplane size of 7 μ m \times 7 μ m and contained at least 100 NWs.

For a given NW ensemble, the evolution of neck area A_n at all the NW junctions was evaluated for a range of dummy temperature histories by using the derived MNCs. The corresponding junction resistivity R_J was updated as a function of junction-specific A_n using eq 11. The ensemble resistivity ρ was then calculated using eq 10. The computed ensemble resistivity was related to the thermal history parameter Θ (eq 8) to yield MRCs of the form shown in eq 12. The values of parameters x and y for a given NW radius were identified from MRCs created for multiple ensembles, for example, for the 25 and 50 nm NW radii used in our experiments. These MRCs allow the direct prediction of ensemble resistivity based on the temperature history from the thermal simulations of the sintering process, as described in the next section.

$$\rho = x + y \ln \Theta \tag{12}$$

2.4. Experimental Validation. The resistivity evolution predicted using our overall framework was validated for the IPL process. In IPL, the incidence of broad-spectrum, highenergy, pulsed light on printed nanoparticles plasmonically heats and sinters them into electrically contiguous structures. The high electrical conductivity, low substrate damage, and high throughput (feet/ms scales) have led to significant interest in this process. Because of the pulsed nature of the IPL light, the use of this process for validating our framework allows us to examine the applicability to nonisothermal sintering conditions. Because the cooling time after the optical pulse is on the order of seconds and the optical pulse itself is on the order of 100 s of microseconds, we are able to examine the ability of our framework to capture longer time scales than that possible with MD simulations. Note that our framework is extensible across a range of thermally driven sintering processes beyond IPL as long as the thermal history is known.

NWs of nominal radii 25 and 50 nm and length 100 μ m were printed as films on polycarbonate substrates using aerosol jet printing, after our previous work. ²⁹ The film thickness, peak film temperature during IPL, film morphology, and the change in resistivity after IPL were measured for varying optical

fluence (Figure S6). Temperature evolution was modeled using thermal FEA from our past work, in which the NW film was modeled as a continuum structure.³⁸ Further details on the experimental and thermal simulation methods are provided in the Methods section.

Figure 7a,b shows that our thermal simulation reasonably predicts the film temperature during IPL. At the same pulse fluence, the peak temperature is greater for the 25 nm radius films because of their greater optical absorptivity over the entire spectrum of the xenon light (Figure S6b). The film's resistivity decreases with increasing pulse fluence up to 6 J/cm² for 25 nm radius films and up to 8 J/cm² for 50 nm radius films (Figure 7c,d). Beyond this radius-specific critical fluence, the film resistivity increases due to blowoff, as shown in past work. 11,13 Figure 7c,d shows that our framework can predict the resistivity within the pulse fluence range corresponding to sintering, thus demonstrating that both the state (temperature) and property (resistivity) can be modeled. Our framework is not valid beyond the sintering range of pulse fluence because the blowoff phenomenon is not considered in our models. Figure 7e shows representative scanning electron microscopy (SEM) images of NW ensembles as a function of the pulse energy used for IPL. We observe local necking of the NWs along their lengths because of atomic diffusion along the length. This phenomenon may affect resistivity but is not incorporated into our model. Given the accuracy of our framework in the sintering regime, it is likely that this lengthwise necking has a relatively lesser effect on resistivity in the sintering regime than that of the inter-NW neck growth.

A significant advantage of our framework is the reduction in the computational effort required. The computational time for the direct use of the analytical neck growth model and the analytical resistivity model for modeling conductivity in the NW ensembles over 1 μ s of sintering time is around 10 h with 64 CPUs. Thus, the computational effort is 640 CPU-h. This effort increases drastically as the size of the ensembles increases to levels relevant to device-scale interconnects and films, and to the ms and second time scales relevant to sintering practice. Using such a modeling approach for the rational design of the process and the NW size is practically infeasible. Our framework builds on the analytical neck growth model and the network resistivity model by converting them into MNCs and MRCs, thus enabling computational times as little as 10 s with 64 CPUs for inch-scale films over sintering times of microseconds to seconds. This corresponds to a computational effort of 0.2 CPU-h, a 4 orders of magnitude reduction compared to the direct use of analytical models and a 10 orders of magnitude reduction as compared to the direct use of MD simulations if that is at all possible. This advantage is complemented by the minimal effort needed for model recalibration for additional NW radii, as follows. The most time-consuming calibration step in our framework is the use of multiple MD simulations to calibrate the analytical neck growth model for different NW diameters. As stated earlier, our successful expression of the model parameters as functions of the NW radii obviates this step during recalibration. The recalibration of the MNCs for specific NW radii takes little time and effort because the underlying analytical neck growth model is computationally fast. Similarly, the recalibration of the MRCs for additional NW radii requires minimal effort because it uses computationally efficient MNCs and analytical network resistivity models along with explicit expressions of junction resistance as a function of the neck area.

The MD simulations performed in our past work, which are the basis for the quantitative calibration of the MNCs, provide a strong energetically motivated foundation for the retention of the qualitative form of the analytical neck growth model and thus of the MNCs across different metallic NW materials.³¹ For brevity, the reader is asked to review the above reference study for further details. The quantitative dependence of MRCs on the specific material of the metal NW is easily incorporated by changing the electrical properties of the NW material in the electromagnetic FEA. Thus, our framework should be extendable across additional metallic NW materials, although with quantitative recalibration of parameters required. The specific model parameters that must be recalibrated when the NW material is changed, and how these parameters can be recalibrated, are now discussed briefly. We do not discuss the changes in fundamental material properties like specific surface energy, atomic volume, and bulk resistivity, which must obviously be changed to match the specific NW material and are obtainable from the literature. The values of the parameters for D_{eff} and Γ in the analytical neck growth model (eqs 6 and 7) will have to be recalibrated as described in the Supporting Information, based on the quantitative evolution of neck growth for the specific NW material, as predicted by additional MD simulations. This calibrated analytical model can be directly used for the recalibration of the parameters $Q_1 \chi_1$ and ϕ for the MNCs, without additional MD simulations. Furthermore, the parameters x and y in the MRCs (eq 12) will have to be recalibrated based on electromagnetic FEA with the correct bulk resistivity of the NW material.

3. CONCLUSIONS

The major contribution of this work is to derive and experimentally validate a hitherto absent multiscale modeling approach that links neck growth and electrical conductivity during the sintering of large multi-NW ensembles under arbitrary temperature profiles. This framework links analytical models of nanoscale neck growth motivated by mechanistic insights from past atomistic simulations, physically grounded master curve representations of neck growth and resistivity as functions of thermal history, and sintering process-specific thermal simulations (e.g., for the IPL process here). Furthermore, the developed MNCs yield new insight into junction-specific neck growth in NW ensembles, showing that a local NW orientation in as-printed ensembles is a key regulator of the corresponding local evolution in neck growth and junction resistivity and therefore in the global evolution of ensemble conductivity. Our framework is also easily extensible to other sintering processes as long as thermal models of the sintering process are available. The reduction in computational effort, easy recalibration for additional NW radii, and mechanistically grounded nature of our framework constitutes a key scientific enabler for the rational design of the sintering process and the NW morphology to achieve desired conductivity under the constraints of thermal damage of the substrate.

4. METHODS

4.1. Experimental Methods. Ag NW inks were prepared by suspending as-received NWs of radii 25 and 50 nm and a nominal length of 100 μ m from ACS Materials in ethanol at a concentration of 5 mg/mL. The inks were deposited on 25 mm \times 25 mm \times 2.5 mm polycarbonate substrates using an aerosol jet printer to create thin films (e.g., Figure S7). The substrate was preheated to 70 °C to

quickly evaporate ethanol during printing. The printing nozzle was fixed at 35 mm height above the substrate. The ink flow rate was 1 mL/min, and the atomizer used compressed air at 0.5 psi to aerosolize the ink. The planar motion of the sample was at a velocity of 50 mm/s and was achieved by motion stages on which the sample was mounted. The number of printing passes was fixed at 100. The printed films were subjected to a single IPL pulse from a xenon lamp (Sinteron 3000 system, Xenon Corporation) with an optical footprint of 1 foot × 1 in. The thin film was kept 1.5 in. away from the focal plane of the lamp, and the lamp voltage was 3 kV. The optical fluence was varied by changing the pulse on time, as shown in Table S2. The sheet resistance was measured using a Keithley source meter and a four-point probe and was converted to resistivity based on the film thickness measured using a Keyence optical profilometer. The film temperature during IPL was measured using a laser pyrometer (Metis-M3, Process Sensors Ltd.). The optical absorption spectra of the films were measured using an ultraviolet-visible (UV-vis) spectrophotometer with an integrating sphere (Jasco Inc., V⁻⁷⁵⁰). SEM (Zeiss Sigma Field Emission 8100) was used to characterize the morphology of the printed NP ensembles before and after IPL. At least four experiments were performed to obtain the standard deviations for a given combination of experimental process parameters.

4.2. Theoretical Methods. The temperature evolution of the film during IPL was simulated using a previously developed thermal finite element model that treats the film as a continuum structure. The material constants used in the thermal model are shown in Table S3. Readers are referred to our previous work³¹ for further details on the MD simulations.

ASSOCIATED CONTENT

Supporting Information

The Supporting Information is available free of charge at https://pubs.acs.org/doi/10.1021/acsami.1c16581.

Derivation of functional expressions for *A*, *B*, *K*; shrinkage rate and rotation rate; neck area comparison between MD simulations and analytical model; temperature history used to validate MNC; example of an NW ensemble for modeling; experimentally measured film thickness and optical absorptivity; exemplar printed NW film; calibrated parameters *x* and *y* for MRCs; FLS parameters; and thermal model parameters (PDF)

AUTHOR INFORMATION

Corresponding Author

Rajiv Malhotra — Department of Mechanical & Aerospace Engineering, Rutgers University, Piscataway, New Jersey 08854, United States; orcid.org/0000-0003-4914-4497; Phone: 1-848-445-5058; Email: rajiv.malhotra@rutgers.edu; Fax: 1-732-445-3124

Authors

Harish Devaraj – Department of Mechanical & Aerospace Engineering, Rutgers University, Piscataway, New Jersey 08854, United States

Qi Tian — Department of Industrial and Systems Engineering, Rutgers University, Piscataway, New Jersey 08854, United States

Weihong Guo – Department of Industrial and Systems Engineering, Rutgers University, Piscataway, New Jersey 08854, United States

Complete contact information is available at: https://pubs.acs.org/10.1021/acsami.1c16581

Notes

The authors declare no competing financial interest.

ACKNOWLEDGMENTS

This work was supported by the National Science Foundation, USA, grant CMMI #2001081.

REFERENCES

- (1) Kim, T. Y.; Shin, S.; Choi, H.; Jeong, S. H.; Myung, D.; Hahn, S. K. Smart Contact Lenses with a Transparent Silver Nanowire Strain Sensor for Continuous Intraocular Pressure Monitoring. ACS Appl. Bio Mater. 2021, 4, 4532–4541.
- (2) Teymouri, A.; Adabifiroozjaei, E.; Webster, R. F.; Hagh, S. M.; Hao, X.; Green, M. A.; Pillai, S. Evidence of Low-Temperature Joints in Silver Nanowire Based Transparent Conducting Layers for Solar Cells. ACS Appl. Nano Mater. 2020, 3, 3205–3213.
- (3) Xu, W.; Zhong, L.; Xu, F.; Shen, W.; Song, W.; Chou, S. Silver Nanowire-Based Flexible Transparent Composite Film for Curvature Measurements. ACS Appl. Nano Mater. 2018, 1, 3859–3866.
- (4) Das, P.; Yeo, C. K.; Ma, J.; Duong Phan, K.; Chen, P.; Chan-Park, M. B.; Duan, H. Nacre Mimetic with Embedded Silver Nanowire for Resistive Heating. ACS Appl. Nano Mater. 2018, 1, 940–952
- (5) Zhou, B.; Li, Q.; Xu, P.; Feng, Y.; Ma, J.; Liu, C.; Shen, C. An Asymmetric Sandwich Structural Cellulose-based Film with Self-supported MXene and AgNW layers for Flexible Electromagnetic Interference Shielding and Thermal Management. *Nanoscale* 2021, 13, 2378–2388.
- (6) Nair, N. M.; Khanra, I.; Ray, D.; Swaminathan, P. Silver Nanowire-Based Printable Electrothermochromic Ink for Flexible Touch-Display Applications. *ACS Appl. Mater. Interfaces* 2021, 13, 34550—34560.
- (7) Neto, J. P.; Costa, A.; Vaz Pinto, J.; Marques-Smith, A.; Costa, J. C.; Martins, R.; Fortunato, E.; Kampff, A. R.; Barquinha, P. Transparent and Flexible Electrocorticography Electrode Arrays Based on Silver Nanowire Networks for Neural Recordings. ACS Appl. Nano Mater. 2021, 4, 5737–5747.
- (8) Yang, G.; Zhang, X.; Pan, D.; Zhang, W.; Shang, Y.; Su, F.; Ji, Y.; Liu, C.; Shen, C. Highly Thermal Conductive Poly(vinyl alcohol) Composites with Oriented Hybrid Networks: Silver Nanowire Bridged Boron Nitride Nanoplatelets. ACS Appl. Mater. Interfaces 2021, 13, 32286–32294.
- (9) Crêpellière, J.; Menguelti, K.; Wack, S.; Bouton, O.; Gérard, M.; Popa, P. L.; Pistillo, B. R.; Leturcq, R.; Michel, M. Spray Deposition of Silver Nanowires on Large Area Substrates for Transparent Electrodes. ACS Appl. Nano Mater. 2021, 4, 1126–1135.
- (10) Kumar, K. S.; Zhang, L.; Kalairaj, M. S.; Banerjee, H.; Xiao, X.; Jiayi, C. C.; Huang, H.; Lim, C. M.; Ouyang, J.; Ren, H. Stretchable and Sensitive Silver Nanowire-Hydrogel Strain Sensors for Proprioceptive Actuation. ACS Appl. Mater. Interfaces 2021, 13, 37816—37829.
- (11) Devaraj, H.; Hwang, H.-J.; Malhotra, R. Understanding the role of Nanomorphology on Resistance Evolution in the Hybrid Form-Fuse Process for Conformal Electronics. *J. Manuf. Process.* 2020, 58, 1088–1102.
- (12) Devaraj, H.; Malhotra, R. Scalable Forming and Flash Light Sintering of Polymer-Supported Interconnects for Surface-Conformal Electronics. *J. Manuf. Sci. Eng.* 2019, 141, No. 041014.
- (13) Jahangir, M. N.; Cleeman, J.; Hwang, H.-J.; Malhotra, R. Towards Out-of-chamber Damage-free Fabrication of Highly Conductive Nanoparticle-based Circuits inside 3D Printed Thermally Sensitive Polymers. *Addit. Manuf.* 2019, 30, No. 100886.
- (14) Qian, F.; Lan, P. C.; Freyman, M. C.; Chen, W.; Kou, T.; Olson, T. Y.; Zhu, C.; Worsley, M. A.; Duoss, E. B.; Spadaccini, C. M.; Baumann, T.; Han, T. Y.-J. Ultralight Conductive Silver Nanowire Aerogels. *Nano Lett.* 2017, 17, 7171–7176.
- (15) Milano, G.; Cultrera, A.; Bejtka, K.; De Leo, N.; Callegaro, L.; Ricciardi, C.; Boarino, L. Mapping Time-Dependent Conductivity of Metallic Nanowire Networks by Electrical Resistance Tomography toward Transparent Conductive Materials. ACS Appl. Nano Mater. 2020, 3, 11987–11997.

- (16) Kang, C.; Yang, S.; Tan, M.; Wei, C.; Liu, Q.; Fang, J.; Liu, G. Purification of Copper Nanowires To Prepare Flexible Transparent Conductive Films with High Performance. ACS Appl. Nano Mater. 2018, 1, 3155–3163.
- (17) Hanauer, S.; Celle, C.; Crivello, C.; Szambolics, H.; Muñoz-Rojas, D.; Bellet, D.; Simonato, J.-P. Transparent and Mechanically Resistant Silver-Nanowire-Based Low-Emissivity Coatings. ACS Appl. Mater. Interfaces 2021, 13, 21971–21978.
- (18) Kim, T.; Kim, Y. W.; Lee, H. S.; Kim, H.; Yang, W. S.; Suh, K. S. Uniformly Interconnected Silver-Nanowire Networks for Transparent Film Heaters. *Adv. Funct. Mater.* 2013, 23, 1250–1255.
- (19) Kwon, J.; Cho, H.; Eom, H.; Lee, H.; Suh, Y. D.; Moon, H.; Shin, J.; Hong, S.; Ko, S. H. Low-Temperature Oxidation-Free Selective Laser Sintering of Cu Nanoparticle Paste on a Polymer Substrate for the Flexible Touch Panel Applications. ACS Appl. Mater. Interfaces 2016, 8, 11575–11582.
- (20) Balliu, E.; Andersson, H.; Engholm, M.; Öhlund, T.; Nilsson, H.-E.; Olin, H. Selective Laser Sintering of Inkjet-printed Silver Nanoparticle Inks on Paper Substrates to Achieve Highly Conductive Patterns. Sci. Rep. 2018, 8, 1–9.
- (21) Rahman, M. T.; Cheng, C.-Y.; Karagoz, B.; Renn, M.; Schrandt, M.; Gellman, A.; Panat, R. High Performance Flexible Temperature Sensors via Nanoparticle Printing. ACS Appl. Nano Mater. 2019, 2, 3280–3291.
- (22) Joo, S.-J.; Park, S.-H.; Moon, C.-J.; Kim, H.-S. A Highly Reliable Copper Nanowire/Nanoparticle Ink Pattern with High Conductivity on Flexible Substrate prepared via a Flash Light-Sintering Technique. ACS Appl. Mater. Interfaces 2015, 7, 5674—5684.
- (23) Jang, Y.-R.; Chung, W.-H.; Hwang, Y.-T.; Hwang, H.-J.; Kim, S.-H.; Kim, H.-S. Selective Wavelength Plasmonic Flash Light Welding Of Silver Nanowires For Transparent Electrodes With High Conductivity. ACS Appl. Mater. Interfaces 2018, 10, 24099—24107.
- (24) Mallikarjuna, K.; Hwang, H.-J.; Chung, W.-H.; Kim, H.-S. Photonic Welding Of Ultra-Long Copper Nanowire Network For Flexible Transparent Electrodes Using White Flash Light Sintering. *RSC Adv.* 2016, 6, 4770–4779.
- (25) Allen, M. L.; Aronniemi, M.; Mattila, T.; Alastalo, A.; Ojanperä, K.; Suhonen, M.; Seppä, H. Electrical Sintering Of Nanoparticle Structures. *Nanotechnology* 2008, *19*, No. 175201.
- (26) Jang, Y.-R.; Joo, S.-J.; Chu, J.-H.; Uhm, H.-J.; Park, J.-W.; Ryu, C.-H.; Yu, M.-H.; Kim, H.-S. A Review On Intense Pulsed Light Sintering Technologies For Conductive Electrodes In Printed Electronics. *Int. J. Precis. Eng. Manuf. Green Technol.* 2020, 8, 1–37.
- (27) Dexter, M.; Pfau, A.; Gao, Z.; Herman, G. S.; Chang, C.-H.; Malhotra, R. Modeling Nanoscale Temperature Gradients And Conductivity Evolution In Pulsed Light Sintering Of Silver Nanowire Networks. *Nanotechnology* 2018, 29, 505205.
- (28) Hwang, H.-J.; Malhotra, R. Shape-Tuned Junction Resistivity and Self-Damping Dynamics in Intense Pulsed Light Sintering of Silver Nanostructure Films. ACS Appl. Mater. Interfaces 2019, 11, 3536–3546.
- (29) Hwang, H.-J.; Devaraj, H.; Yang, C.; Gao, Z.; Chang, C.-H.; Lee, H.; Malhotra, R. Rapid Pulsed Light Sintering Of Silver Nanowires On Woven Polyester For Personal Thermal Management With Enhanced Performance, Durability And Cost-Effectiveness. *Sci. Rep.* 2018, *8*, 17159.
- (30) Lagrange, M.; Langley, D. P.; Giusti, G.; Jiménez, C.; Bréchet, Y.; Bellet, D. Optimization Of Silver Nanowire-Based Transparent Electrodes: Effects Of Density, Size And Thermal Annealing. *Nanoscale* 2015, 7, 17410–17423.
- (31) Jahangir, M. N.; Devaraj, H.; Malhotra, R. On Self-Limiting Rotation and Diffusion Mechanisms during Sintering of Silver Nanowires. *J. Phys. Chem. C* 2020, 124, 19849–19857.
- (32) Jagota, M.; Tansu, N. Conductivity Of Nanowire Arrays Under Random And Ordered Orientation Configurations. *Sci. Rep.* 2015, *5*, 1–5.

- (33) Forró, C.; Demkó, L.; Weydert, S.; Vörös, J. N.; Tybrandt, K. Predictive Model For The Electrical Transport Within Nanowire Networks. ACS Nano 2018, 12, 11080–11087.
- (34) Nirmalraj, P. N.; Bellew, A. T.; Bell, A. P.; Fairfield, J. A.; McCarthy, E. K.; O'Kelly, C.; Pereira, L. F.; Sorel, S.; Morosan, D.; Coleman, J. N. Manipulating Connectivity And Electrical Conductivity In Metallic Nanowire Networks. *Nano Lett.* 2012, 12, 5966–5971.
- (35) Borchert, J. W.; Stewart, I. E.; Ye, S.; Rathmell, A. R.; Wiley, B. J.; Winey, K. I. Effects Of Length Dispersity And Film Fabrication On The Sheet Resistance Of Copper Nanowire Transparent Conductors. *Nanoscale* 2015, 7, 14496–14504.
- (36) Langley, D.; Lagrange, M.; Giusti, G.; Jiménez, C.; Bréchet, Y.; Nguyen, N. D.; Bellet, D. Metallic Nanowire Networks: Effects Of Thermal Annealing On Electrical Resistance. *Nanoscale* 2014, 6, 13535–13543.
- (37) MacNeill, W.; Choi, C.-H.; Chang, C.-H.; Malhotra, R. On The Self-Damping Nature Of Densification In Photonic Sintering Of Nanoparticles. Sci. Rep. 2015, 5, 14845.
- (38) Bansal, S.; Malhotra, R. Nanoscale-Shape-Mediated Coupling Between Temperature And Densification In Intense Pulsed Light Sintering. *Nanotechnology* 2016, 27, No. 495602.
- (39) Dyke, M. V. Perturbation Methods in Fluid Mechanics. *Nature* 1965, 206, 226–227.
- (40) Johnson, D. L. New Method of Obtaining Volume, Grain-Boundary, and Surface Diffusion Coefficients from Sintering Data. *J. Appl. Phys.* 1969, 40, 192–200.
- (41) Parhami, F.; McMeeking, R. M. A Network Model For Initial Stage Sintering. *Mech. Mater.* 1998, 27, 111–124.
- (42) Castro, R.; Benthem, K., Sintering: Mechanisms of Convention Nanodensification and Field Assisted Processes; Springer Publishing, 2013; pp 17–34.
- (43) Hardy, G.; Seshu Aiyan, P.; Wilson, B., Collected Papers of Srinivasa Ramanujan; Chelsea Pub Co., 1927; pp 426.
- (44) Swinkels, F. B.; Ashby, M. F. A Second Report on Sintering Diagrams. Acta Metall. 1981, 29, 259-281.
- (45) Parhami, F.; McMeeking, R. M.; Cocks, A. C. F.; Suo, Z. A Model For The Sintering And Coarsening Of Rows Of Spherical Particles. *Mech. Mater.* 1999, 31, 43–61.
- (46) Kim, D.; Nam, J. Systematic Analysis For Electrical Conductivity Of Network Of Conducting Rods By Kirchhoff's Laws And Block Matrices. J. Appl. Phys. 2018, 124, 215104.
- (47) Manca, J. V.; Croes, K.; De Ceuninck, W.; D'Haeger, V.; D'Haen, J.; Depauw, P.; Tielemans, L.; De Schepper, L. Localized Monitoring Of Electromigration With Early Resistance Change Measurements. *Microelectron. Reliab.* 1998, 38, 641–650.
- (48) Zhou, J. H.; Zhang, Y. W.; Chen, J. K. Numerical Simulation of Random Packing of Spherical Particles for Powder-Based Additive Manufacturing. *J. Manuf. Sci. Eng.* 2009, 131, No. 031004.